Layer-wise numerical model for laminated glass plates with viscoelastic interlayer

Alena Zemanová*, Jan Zeman[a], Tomáš Janda[b] and Michal Šejnoha[c]

*Department of Mechanics, Faculty of Civil Engineering, Czech Technical University in Prague,
Thákurova 7, 166 29 Prague 6, Czech Republic*

Abstract. In this paper, a multi-layered finite element model for laminated glass plates is introduced. A layer-wise theory is applied to the analysis of laminated glass due to the combination of stiff and soft layers; the independent layers are connected via Lagrange multipliers. The von Kármán large deflection plate theory and the constant Poisson ratio for constitutive equations are assumed to capture the possible effects of geometric nonlinearity and the time/temperature-dependent response of the plastic foil. The linear viscoelastic behavior of a polymer foil is included by the generalized Maxwell model. The proposed layer-wise model was implemented into the MATLAB code and verified against detailed three-dimensional models in ADINA solver using different hexahedral finite elements. The effects of temperature, load duration, and creep/relaxation are demonstrated by examples.

Keywords: laminated glass plate; finite element method; layer-wise plate model; Lagrange multipliers; geometric nonlinearity; von Kármán assumptions; time/temperature-dependent behavior; generalized Maxwell model, Williams-Landel-Ferry equation; Newton method

1. Introduction

Due to its high optical quality, laminated glass is an important material for safe transparent elements in the automobile, aircraft, and civil engineering industries. The lamination of brittle glass with a ductile interlayer, typically made of polymer foil, significantly improves the post-fracture behavior of the member; on the other hand, it also affects the response of unfractured laminated glass plate because the foil is time/temperature-dependent (Huang *et al.* 2014) and soft (the glass-to-polymer stiffness ratio is 10^3 or greater). Moreover, laminated glass plates are very slender, and therefore the effect of geometric nonlinearity can be significant (Xenidis *et al.* 2015). All these aspects should be captured in analysis of laminated glass structures. Numerous theories for laminated composite plates have been developed and reported in literature; a general review of numerical models is provided by e.g., (Reddy and Robbins 1994), (Carrera 2002), or (Zhang and Yang, 2009). A more specific overview of numerical approaches for laminated glass plates can be found in (Liang *et al.* 2016), (Eisenträger *et al.* 2015a), or (Eisenträger *et al.* 2015b). Generally, these methods can be broadly divided into the following categories:

  • effective thickness or stiffness approaches,
  • layer-wise (or multi-layered) theories, and
  • detailed models based on 3D continuum theories.

For plate structures, a closed form analytical solution is possible for specific boundary conditions and loading, such as a simply-supported plate strip under uniformly distributed tangential loading in (Naumenko and Eremeyev 2014) for arbitrary boundary conditions, only approximate analytical solutions can be derived, (Wu *et al.* 2016), and numerical techniques are preferred. In *effective thickness approaches*, a reduced thickness of a monolith with equivalent bending properties in terms of the largest value of deflection or stress is derived; the effective thickness expressions for plate structures can be found for example in (Galuppi and Royer-Carfagni 2012). The results of some of those relatively undemanding single-layer approaches are not always on the side of safety or these methods can overestimate the deflection for very soft core layers (Eisenträger *et al.* 2015a). However, some of them may provide a precise prediction of the behavior of laminated glass, see the comparison in (Galuppi and Royer-Carfagni 2013a) for a static loading and in (Schmidt *et al.* 2017) for a dynamic analysis.

On the other hand, *detailed 3D numerical simulations* are computationally expensive because they require a large number of elements due to the large span/thickness ratio of laminated plates. *Layer-wise theories* provide sufficiently accurate stresses and strains distributions at the ply levels, and can reduce the computational cost, which will be discussed in this paper. *Zig-zag theories* stand in between effective thickness and layer-wise approaches. The in-plane displacements are expanded over the cross-section by adopting a piecewise linear (zig-zag) function; for more details see (Carrera 2004). These methods give relatively

─────────────────

*Corresponding author, Ph.D.
  E-mail: alena.zemanova@fsv.cvut.cz
[a]Associate Professor
[b]Ph.D.
[c]Professor

low-cost, accurate estimates of structural response and are well-suited for laminated plates with a higher number of layers.

Regarding the material model for polymer foil, the majority of the approaches available in literature assume the elastic behavior of interlayer material because the time/temperature-dependent iterative solution increases the computational cost even more. One of the first analyses accounting for the time/temperature-dependency of polymer foil behavior can be found in (Duser *et al.* 1999) belonging to the last group of detail numerical 3D simulations; a recent paper by (Liang *et al.* 2016) is an example of a zig-zag model including the relaxation effects for interlayer material. In both of them, the polymer foil is assumed as a linear viscoelastic material with *the constant bulk modulus*.

The objective of this paper is the formulation of a finite element model for laminated glass plates taking into account the time/temperature dependency of polymer foil behavior and geometrically nonlinear effects, its verification against detailed 3D solid model in an established finite element solver, and a brief parametric study. The proposed viscoelastic formulation is an extension of the elastic one for laminated glass plates from (Zemanová *et al.* 2015), and it belongs to the group of layer-wise approaches. We decided to treat each layer independently because this scheme can be naturally extended towards the post-fracture response when individual glass layers are fractured. Moreover, the Lagrange multipliers (with a physical meaning of nodal forces holding the neighboring layers together) offer a convenient way to capture possible delamination, which can occur during a post-fracture stage or due to a low velocity impact (Flocker and Dharani 1998). However, this contribution analyzes unfractured plates in bending under static loading, therefore no delamination is assumed in this paper. Unlike other authors, we assume *the constant Poisson ratio* in our viscoelastic formulation for the polymer interlayer in a laminated glass plate. This results in easier formulation but gives the same results for laminated glass structures as shown in (Zemanová *et al.* 2017).

The structure of this paper is as follows. In Section 2, the variational formulation for a laminated glass plate with time/temperature-dependent behavior of interlayers is introduced, starting from kinematic and constitutive assumptions and relations. Then, the energy functional is derived, discretized, and the solution procedure is outlined. In Section 3, the layer-wise model is verified against 3D simulations in ADINA solver, its convergence and computational cost is discussed, and the effects of temperature, loading duration, and relaxation are studied and demonstrated by examples. Conclusions from this comparison are made in Section 4. Finally, the detailed derivation of the nodal internal forces and the stiffness matrix can be found in Appendix A.

2. Formulation of viscoelastic model for laminated glass plate

Models for laminated glass beams under different kinematic and constitutive assumptions were derived and
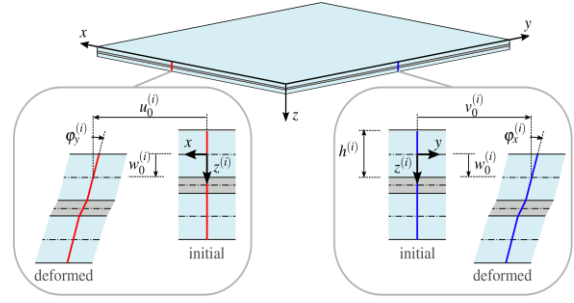

Fig. 1 Scheme of a three-layer laminated glass plate with kinematic variables for the top layer ($i = 1$)

compared in (Zemanová *et al.* 2017), and the conclusions are used for the laminated glass plate formulation.

• The finite element model is based on the refined laminated plate theory by (Mau 1973). The plate consists of N layers. Each layer has independent kinematics, and the compatibility conditions are ensured via *Lagrange multipliers*.

• Due to the combination of stiff and soft material, non-negligible shear strains occur in the polymer interlayer. These shear strains are accounted in a simple way via *the shear deformable Reissner-Mindlin plate theory* (also the first-order shear deformation theory of plates) applied for each layer independently and complemented with *the von Kármán assumptions* for large deflections.[1]

• For constitutive equations, *the constant Poisson ratio* is assumed for viscoelastic behavior of foil whereas the glass layers behave in an elastic manner.

The following nomenclature is used in the text. Scalar quantities are denoted by lightface letters and the bold letters are reserved for matrices. The Cartesian coordinate system is set on each mid-surface of an undeformed layer so that the in-plane coordinates x and y are the same for all layers, whereas out-of-plane coordinate $z^{(i)}$ is associated with the i-th layer (the zero value is set in the middle of this layer). However, the formulation is valid in general, we discuss and verify the most common case of laminated glass plates with three layers (glass/interlayer/glass) in this paper. The time-dependence of a quantity is denoted as $\bullet(t_n)$ or $\bullet(t_{n+1})$; if convenient, it is shortened as $\bullet_n$ or $\bullet_{n+1}$.

In order to avoid a profusion of notation, we omit the dependence of quantities of interest on the time variable t in Section 2.1 because the equations are valid also for elastic layers, while in Section 2.2 we omit the layer index $\bullet^{(i)}$ because the constitutive description holds only for the interlayer.

2.1 Kinematics

Under the von Kármán assumptions, the membrane displacements $\mathbf{u}^{(i)} = [u^{(i)}, v^{(i)}]^{\mathrm{T}}$ are treated as small whereas the transverse displacements $w^{(i)}$ as large. The equations for the displacement field

---

[1] A comparison of the von Kármán large deflection model with the finite-strain Reissner model for laminated glass beams can be found in (Zemanová *et al.* 2017).

$$\mathbf{u}^{(i)}\big(x,y,z^{(i)}\big) = \mathbf{u}_0^{(i)}(x,y) + \mathbf{S}\boldsymbol{\varphi}^{(i)}(x,y)z^{(i)},$$

$$w^{(i)}\big(x,y,z^{(i)}\big) = w_0^{(i)}(x,y), \tag{1}$$

are composed of the displacements of the mid-surface $\mathbf{u}_0^{(i)} = [u_0^{(i)}, v_0^{(i)}]^{\mathrm{T}}$ complemented with the contribution of the straight line segment rotations about corresponding axis $\boldsymbol{\varphi}^{(i)} = [\varphi_x^{(i)}, \varphi_y^{(i)}]^{\mathrm{T}}$, where matrix $\mathbf{S} = [0,1;-1,0]$, and the mid-surface deflection $w_0^{(i)}$, Fig. 1.

The compatibility conditions of the displacements across interfaces

$$\mathbf{c}^{(i,i+1)}(x,y) = \mathbf{u}^{(i)}\left(x,y,\frac{h^{(i)}}{2}\right) - \mathbf{u}^{(i+1)}\left(x,y,-\frac{h^{(i)}}{2}\right),$$

$$\mathbf{c}^{(i,i+1)}(x,y) = \mathbf{0},$$

$$c_z^{(i,i+1)}(x,y) = w^{(i)}\left(x,y,\frac{h^{(i)}}{2}\right)$$

$$- w^{(i+1)}\left(x,y,-\frac{h^{(i)}}{2}\right), \tag{2}$$

$$c_z^{(i,i+1)}(x,y) = 0$$

correspond to the assumption of a perfect bond of neighboring layers (for a three-layered plate $i = 1,2$).

The strains field is composed of the membrane components $\boldsymbol{\varepsilon}_m^{(i)} = [\varepsilon_x^{(i)}, \varepsilon_y^{(i)}, \gamma_{xy}^{(i)}]^{\mathrm{T}}$ and the transverse shear strains $\boldsymbol{\gamma}^{(i)} = [\gamma_{xz}^{(i)}, \gamma_{yz}^{(i)}]^{\mathrm{T}}$,

$$\boldsymbol{\varepsilon}_m^{(i)}(x,y,z^{(i)}) = \boldsymbol{\varepsilon}_{m0}^{(i)}(x,y) + \boldsymbol{\kappa}^{(i)}(x,y)z^{(i)},$$

$$\boldsymbol{\gamma}^{(i)}(x,y) = \nabla w_0^{(i)}(x,y) + \mathbf{S}\boldsymbol{\varphi}^{(i)}(x,y). \tag{3}$$

The mid-surface membrane strains

$$\boldsymbol{\varepsilon}_{m0}^{(i)}(x,y) = \boldsymbol{\partial}\mathbf{u}_0^{(i)}(x,y) + \boldsymbol{\varepsilon}_K^{(i)}(x,y) \tag{4}$$

include also the nonlinear contributions, which depend only on the deflections

$$\boldsymbol{\varepsilon}_K^{(i)}(x,y) = \begin{bmatrix} \frac{1}{2}\left(\frac{\partial w_0^{(i)}}{\partial x}(x,y)\right)^2 \\ \frac{1}{2}\left(\frac{\partial w_0^{(i)}}{\partial y}(x,y)\right)^2 \\ \frac{\partial w_0^{(i)}}{\partial x}(x,y)\frac{\partial w_0^{(i)}}{\partial y}(x,y) \end{bmatrix}. \tag{5}$$

The pseudo-curvatures $\boldsymbol{\kappa}^{(i)} = [\kappa_x^{(i)}, \kappa_y^{(i)}, \kappa_{xy}^{(i)}]^{\mathrm{T}}$ are provided by

$$\boldsymbol{\kappa}^{(i)}(x,y) = \boldsymbol{\partial}\mathbf{S}\boldsymbol{\varphi}^{(i)}(x,y), \tag{6}$$

and the differential operators read $\nabla = [\frac{\partial}{\partial x}, \frac{\partial}{\partial y}]^{\mathrm{T}}$ and $\boldsymbol{\partial} = [\frac{\partial}{\partial x}, 0; 0, \frac{\partial}{\partial y}; \frac{\partial}{\partial y}, \frac{\partial}{\partial x}]$.

2.2 Constitutive relations

Glass is supposed to behave in an elastic manner like in (Zemanová *et al.* 2015). Therefore, the following constitutive description holds only for the interlayer; the

layer index $\bullet^{(2)}$ is, thus, omitted in this section to shorten the notation.

2.2.1 Time/temperature-dependent behavior of polymer foil

At the time t, the stress vector at the material point $\boldsymbol{\sigma}(t) = [\sigma_x(t), \sigma_y(t), \sigma_z(t), \tau_{xy}(t), \tau_{xz}(t), \tau_{yz}(t)]^{\mathrm{T}}$ can be expressed from the smooth strain history $\boldsymbol{\varepsilon}(t) = [\varepsilon_x(t), \varepsilon_y(t), \varepsilon_z(t), \gamma_{xy}(t), \gamma_{xz}(t), \gamma_{yz}(t)]^{\mathrm{T}}$ with $\boldsymbol{\varepsilon}(0) = 0$ assuming the constant Poisson ratio as

$$\boldsymbol{\sigma}(t) = \overline{\mathbf{D}}_\nu \int_0^t G(t-t')\frac{\mathrm{d}\boldsymbol{\varepsilon}}{\mathrm{d}t'}(t')\mathrm{d}t', \tag{7}$$

where the matrix $\overline{\mathbf{D}}_\nu$ is given by

$$\overline{\mathbf{D}}_\nu = \begin{bmatrix} \frac{2(1-\nu)}{1-2\nu} & \frac{2\nu}{1-2\nu} & \frac{2\nu}{1-2\nu} & 0 & 0 & 0 \\ \frac{2\nu}{1-2\nu} & \frac{2(1-\nu)}{1-2\nu} & \frac{2\nu}{1-2\nu} & 0 & 0 & 0 \\ \frac{2\nu}{1-2\nu} & \frac{2\nu}{1-2\nu} & \frac{2(1-\nu)}{1-2\nu} & 0 & 0 & 0 \\ 0 & 0 & 0 & 1 & 0 & 0 \\ 0 & 0 & 0 & 0 & 1 & 0 \\ 0 & 0 & 0 & 0 & 0 & 1 \end{bmatrix}. \tag{8}$$

The shear relaxation modulus of the generalized Maxwell chain can be represented by the Prony series, page 32 in (Christensen 1982),

$$G(t-t') = G_\infty + \sum_{p=1}^P G_p\left(\exp^{-\frac{t-t'}{\theta_p}}\right)$$

$$= G_0 - \sum_{p=1}^P G_p\left(1 - \exp^{-\frac{t-t'}{\theta_p}}\right), \tag{9}$$

where P is the number of viscoelastic units, G_p denotes the shear modulus of the p-th unit, $\theta_p = \eta_p/G_p$ is its relaxation time related to the viscosity η_p, G_∞ the shear modulus of the elastic spring, and $G_0 = G_\infty + \sum_{p=1}^P G_p$ the instantaneous shear modulus of the chain.

The true time t_{true} is replaced by the adjusted value $t = t_{\mathrm{true}}/a_T$ taking into account the temperature dependence of the shear modulus of the interlayer. According to the time-temperature superposition principle (Williams *et al.* 1955), the time duration is modified by the temperature-dependent shift function a_T

$$\log a_T = -\frac{C_1(T-T_0)}{C_2 + T - T_0}, \tag{10}$$

where C_1 and C_2 are material constants, and T and T_0 are the current and reference temperatures, respectively.

2.2.2 Incremental formulation at material point

According to the exponential algorithm by (Zienkiewicz *et al.* 1968), we decompose the time interval of interest $\langle 0; t_{\max}\rangle$ into non-equidistant time instants. The goal is to determine the stresses at the end of the time interval $\langle t_n; t_{n+1}\rangle$

$$\boldsymbol{\sigma}_{n+1} = \boldsymbol{\sigma}_n + \Delta\boldsymbol{\sigma}, \tag{11}$$

when the values $\boldsymbol{\sigma}_n$ at the beginning of the time step are known and the strains vary linearly over the time interval.

The increments of the stresses between the time instants t_n and t_{n+1} are written as

$$\Delta\boldsymbol{\sigma} = \overline{\mathbf{D}}_v \hat{G} \Delta\boldsymbol{\varepsilon} + \Delta\hat{\boldsymbol{\sigma}}, \tag{12}$$

where the effective shear modulus over the time interval is expressed by the series

$$\hat{G} = G_\infty + \sum_{p=1}^{P} G_p \frac{\theta_p}{\Delta t} \left(1 - \exp^{-\frac{\Delta t}{\theta_p}}\right) \tag{13}$$

and the stress relaxation effects are represented by

$$\Delta\hat{\boldsymbol{\sigma}} = \sum_{p=1}^{P} \Delta\hat{\boldsymbol{\sigma}}_p = -\sum_{p=1}^{P} \boldsymbol{\sigma}_p(t_n)\left(1 - \exp^{-\frac{\Delta t}{\theta_p}}\right). \tag{14}$$

2.2.3 Specific internal forces increments for plates

For the assumed plane stress state, the normal stress component $\sigma_z = 0$ and the nonzero increments can be decomposed into the membrane stress components $\Delta\boldsymbol{\sigma}_m = [\Delta\sigma_x, \Delta\sigma_y, \Delta\tau_{xy}]^T$ and the shear stress components $\Delta\boldsymbol{\tau} = [\Delta\tau_{xz}, \Delta\tau_{yz}]^T$,

$$\Delta\boldsymbol{\sigma}_m = \overline{\mathbf{D}}_m \hat{G} \Delta\boldsymbol{\varepsilon}_m + \Delta\hat{\boldsymbol{\sigma}}_m, \quad \Delta\boldsymbol{\tau} = \mathbf{I}\hat{G}\Delta\boldsymbol{\gamma} + \Delta\hat{\boldsymbol{\tau}}, \tag{15}$$

where the membrane and shear relaxation effects $\Delta\hat{\boldsymbol{\sigma}}_m$ and $\Delta\hat{\boldsymbol{\tau}}$ are computed according to Eq. (14). The split of matrix $\overline{\mathbf{D}}_v$ in Eq. (8) gives rise to an identity matrix $\mathbf{I}$ and the matrix

$$\overline{\mathbf{D}}_m = \frac{2(1+v)}{1-v^2}\begin{bmatrix} 1 & v & 0 \\ v & 1 & 0 \\ 0 & 0 & \frac{(1-v)}{2} \end{bmatrix}. \tag{16}$$

According to the first-order shear deformation theory for plates, we assume the constant shear stress increments $\Delta\boldsymbol{\tau}$ through the thickness of a layer. The membrane stress increments $\Delta\boldsymbol{\sigma}_m$ are split into the stress increments due to the membrane forces $\Delta\boldsymbol{\sigma}_m^n$ and the stress-gradient increments due to the bending $\Delta\boldsymbol{\sigma}_m^m$

$$\begin{aligned} \Delta\boldsymbol{\sigma}_m(z) &= \Delta\boldsymbol{\sigma}_m^n + \Delta\boldsymbol{\sigma}_m^m z \\ &= \left(\overline{\mathbf{D}}_m \hat{G} \Delta\boldsymbol{\varepsilon}_{m0} + \Delta\hat{\boldsymbol{\sigma}}_m^n\right) \\ &\quad + \left(\overline{\mathbf{D}}_m \hat{G} \Delta\boldsymbol{\kappa} + \Delta\hat{\boldsymbol{\sigma}}_m^m\right)z. \end{aligned} \tag{17}$$

The increments of the specific normal forces $\Delta\mathbf{n} = [\Delta n_x, \Delta n_y, \Delta n_{xy}]^T$, the specific bending moments $\Delta\mathbf{m} = [\Delta m_x, \Delta m_y, \Delta m_{xy}]^T$, and the specific shear forces $\Delta\mathbf{v} = [\Delta v_x, \Delta v_y]^T$ are provided by

$$\begin{aligned} \Delta\mathbf{n}(x,y) &= h\overline{\mathbf{D}}_m \hat{G} \Delta\boldsymbol{\varepsilon}_{m0}(x,y) + \int_h \Delta\hat{\boldsymbol{\sigma}}_m^n(x,y)\mathrm{d}z \\ &= h\overline{\mathbf{D}}_m \hat{G} \Delta\boldsymbol{\varepsilon}_{m0}(x,y) + \Delta\hat{\mathbf{n}}(x,y), \end{aligned} \tag{18}$$

$$\begin{aligned} \Delta\mathbf{m}(x,y) &= \frac{h^3}{12}\overline{\mathbf{D}}_m \hat{G} \Delta\boldsymbol{\kappa}(x,y) + \int_h \Delta\hat{\boldsymbol{\sigma}}_m^m(x,y)z\mathrm{d}z \\ &= \frac{h^3}{12}\overline{\mathbf{D}}_m \hat{G} \Delta\boldsymbol{\kappa}(x,y) + \Delta\hat{\mathbf{m}}(x,y), \end{aligned}$$

$$\begin{aligned} \Delta\mathbf{v}(x,y) &= hk\mathbf{I}\hat{G}\Delta\boldsymbol{\gamma}(x,y) + k\int_h \Delta\hat{\boldsymbol{\tau}}(x,y)\mathrm{d}z \\ &= hk\mathbf{I}\hat{G}\Delta\boldsymbol{\gamma}(x,y) + \Delta\hat{\mathbf{v}}(x,y), \end{aligned}$$

where h is the layer thickness, k is the shear correction factor, see Chapter 13 in (Zienkiewicz *et al.* 2013), and the increments of the specific internal forces due to relaxation are expressed as

$$\Delta\hat{\mathbf{n}} = h\Delta\hat{\boldsymbol{\sigma}}_m^n, \quad \Delta\hat{\mathbf{m}} = \frac{h^3}{12}\Delta\hat{\boldsymbol{\sigma}}_m^m, \quad \Delta\hat{\mathbf{v}} = hk\Delta\hat{\boldsymbol{\tau}}, \tag{19}$$

where the stress increments due to relaxation follow from Eqs. (14) and (17).

2.3 Variational formulation and finite element implementation

2.3.1 Energy functional

The governing equations are derived by minimizing the potential energy functional. The total energy of the laminated plate is the sum of the internal and external component of the potential energy of individual layers, see (Zemanová *et al.* 2015). For a three-layered system at the time t_{n+1}, we get

$$\Pi_{n+1} = (\Pi_{int}^{(1)} + \Pi_{int,n+1}^{(2)} + \Pi_{int}^{(3)}) + \sum_{i=1}^{3} \Pi_{ext}^{(i)}, \tag{20}$$

where $\Pi_{ext}^{(i)}$ is the potential energy of external loading acting on the i-th layer at the time t_{n+1} and $\Pi_{int}^{(i)}$ is the internal energy of the i-th layer.

For elastic glass layers ($i = 1,3$) with the mid-surface $\Omega^{(i)}$

$$\begin{aligned} &\Pi_{int}^{(i)}\left(\mathbf{u}_0^{(i)}, w_0^{(i)}, \boldsymbol{\varphi}^{(i)}\right) \\ &= \frac{1}{2}\int_{\Omega^{(i)}} \left(\boldsymbol{\varepsilon}_{m0}^{(i)}\left(\mathbf{u}_0^{(i)}, w_0^{(i)}\right)\right)^T h^{(i)}\overline{\mathbf{D}}_m^{(i)} G^{(i)}\boldsymbol{\varepsilon}_{m0}^{(i)}\left(\mathbf{u}_0^{(i)}, w_0^{(i)}\right) \\ &+ \left(\boldsymbol{\kappa}^{(i)}\left(\boldsymbol{\varphi}^{(i)}\right)\right)^T \frac{\left(h^{(i)}\right)^3}{12}\overline{\mathbf{D}}_m^{(i)} G^{(i)}\boldsymbol{\kappa}^{(i)}\left(\boldsymbol{\varphi}^{(i)}\right) \\ &+ \left(\boldsymbol{\gamma}^{(i)}\left(w_0^{(i)}, \boldsymbol{\varphi}^{(i)}\right)\right)^T h^{(i)}k^{(i)}\mathbf{I}G^{(i)}\boldsymbol{\gamma}^{(i)}\left(w_0^{(i)}, \boldsymbol{\varphi}^{(i)}\right)\mathrm{d}\Omega^{(i)}. \end{aligned} \tag{21}$$

Due to the viscoelastic behavior of foil, the potential energy of the interlayer ($i = 2$) has to be computed incrementally. The internal potential energy at the time t_{n+1}

$$\begin{aligned} &\Pi_{int,n+1}^{(2)}\left(\mathbf{u}_0^{(2)}, w_0^{(2)}, \boldsymbol{\varphi}^{(2)}\right) \\ &= \Pi_{int,n}^{(2)} + \Delta\Pi_{int}^{(2)}\left(\mathbf{u}_0^{(2)}, w_0^{(2)}, \boldsymbol{\varphi}^{(2)}\right) \end{aligned} \tag{22}$$

consists of the constant value of the internal potential

energy $\Pi_{int,n}^{(2)}$ from the previous time t_n (with $\Pi_{int,0}^{(2)} = 0$ for $t_0 = 0$) and the increment of the internal potential energy

$$
\begin{aligned}
\Delta\Pi_{int}^{(2)}&\left(\mathbf{u}_0^{(2)}, w_0^{(2)}, \boldsymbol{\varphi}^{(2)}\right) \\
&= \int_{\Omega^{(2)}} \left(\Delta\boldsymbol{\varepsilon}_{m0}^{(2)}\left(\mathbf{u}_0^{(2)}, w_0^{(2)}\right)\right)^{\mathrm{T}} \frac{h^{(2)}}{2} \overline{D}_m^{(2)} \hat{G}^{(2)} \Delta\boldsymbol{\varepsilon}_{m0}^{(2)}\left(\mathbf{u}_0^{(2)}, w_0^{(2)}\right) \\
&\quad + \left(\mathbf{n}_n^{(2)} + \Delta\hat{\mathbf{n}}^{(2)}\right)^{\mathrm{T}} \Delta\boldsymbol{\varepsilon}_{m0}^{(2)}\left(\mathbf{u}_0^{(2)}, w_0^{(2)}\right) \\
&\quad + \left(\Delta\boldsymbol{\kappa}^{(2)}\left(\boldsymbol{\varphi}^{(2)}\right)\right)^{\mathrm{T}} \frac{\left(h^{(2)}\right)^3}{24} \overline{D}_m^{(2)} \hat{G}^{(2)} \Delta\boldsymbol{\kappa}^{(2)}\left(\boldsymbol{\varphi}^{(2)}\right) \\
&\quad + \left(\mathbf{m}_n^{(2)} + \Delta\hat{\mathbf{m}}^{(2)}\right)^{\mathrm{T}} \Delta\boldsymbol{\kappa}^{(2)}\left(\boldsymbol{\varphi}^{(2)}\right) \\
&\quad + \left(\Delta\boldsymbol{\gamma}^{(2)}\left(w_0^{(2)}, \boldsymbol{\varphi}^{(2)}\right)\right)^{\mathrm{T}} \frac{h^{(2)}}{2} k^{(2)} \mathbf{I} \hat{G}^{(2)} \Delta\boldsymbol{\gamma}^{(2)}\left(w_0^{(2)}, \boldsymbol{\varphi}^{(2)}\right) \\
&\quad + \left(\mathbf{v}_n^{(2)} + \Delta\hat{\mathbf{v}}^{(2)}\right)^{\mathrm{T}} \Delta\boldsymbol{\gamma}^{(2)}\left(w_0^{(2)}, \boldsymbol{\varphi}^{(2)}\right) \mathrm{d}\Omega^{(2)}.
\end{aligned}
\tag{23}
$$

The shear correction factor k was assumed 5/6 for the glass layers and 1 for the interlayer, because we achieved the best agreement with the response of detailed two-dimensional model from the ADINA solver for laminated glass beams for these values, see (Zemanová *et al.* 2017).

2.3.2 Discretization

The domain of each layer $\Omega^{(i)}$ is discretized with finite elements $\Omega_e^{(i)}$. Then, the internal and external energy is approximated and the total potential energy for an arbitrary kinematically admissible vector of all generalized nodal displacements $\mathbf{d}$ holds

$$
\begin{aligned}
\Pi_{n+1}(\mathbf{d}) = \sum_{e=1}^{N_e} \Bigg(&\sum_{i=1,3} \Pi_{int,e}^{(i)}\left(\mathbf{d}_e^{(i)}\right) \\
&+ \Pi_{int,n+1}^{(2)}\left(\mathbf{d}_e^{(2)}\right) \\
&+ \sum_{i=1}^{3} \Pi_{ext,e}^{(i)}\left(\mathbf{d}_e^{(i)}\right) \Bigg),
\end{aligned}
\tag{24}
$$

where the internal potential energy of the second layer of the e-th element $\Pi_{int,e}^{(2)}$ is computed from the previous time level according to discretized form of Eq. (23). For bilinear approximations of unknown fields, the vector of generalized nodal displacements $\mathbf{d}_e^{(i)}$ for the e-th four-node quadrilateral element of the i-th layer consists of four vectors

$$
\mathbf{d}_j^{(i)} = [u_{0,j}^{(i)}, v_{0,j}^{(i)}, w_{0,j}^{(i)}, \varphi_{x,j}^{(i)}, \varphi_{y,j}^{(i)}]^{\mathrm{T}},
\tag{25}
$$

where j acquires four different numbers belonging to the nodes of the e-th element.

2.3.3 Lagrange function and Karush-Kuhn-Tucker optimality conditions

The Lagrange function for arbitrary kinematically admissible generalized nodal displacements $\mathbf{d}$ at the time t_{n+1}

$$
\mathcal{L}_{n+1}(\mathbf{d}, \boldsymbol{\lambda}) = \Pi_{n+1}(\mathbf{d}) + \boldsymbol{\lambda}^{\mathrm{T}} \mathbf{C}\mathbf{d},
\tag{26}
$$

includes the discretized total potential energy, Eq. (24), and the complementary conditions enforcing the compatibility

$\mathbf{c} = \mathbf{C}\mathbf{d} = \mathbf{0}$, Eq. (2), discretely at all corresponding nodes. The vector $\boldsymbol{\lambda}$ represents the admissible Lagrange multipliers (forces linking the neighboring layers) and the block of matrix $\mathbf{C}$ associated with j-th node has the form

$$
\mathbf{C}_j^{(i,i+1)} = \begin{bmatrix} 1 & 0 & 0 & 0 & \frac{h^{(i)}}{2} & \dots & -1 & 0 & 0 & 0 & \frac{h^{(i+1)}}{2} \\ 0 & 1 & 0 & -\frac{h^{(i)}}{2} & 0 & \dots & 0 & -1 & 0 & -\frac{h^{(i+1)}}{2} & 0 \\ 0 & 0 & 1 & 0 & 0 & \dots & 0 & 0 & -1 & 0 & 0 \end{bmatrix}.
\tag{27}
$$

The vectors of true nodal degrees of freedom $\mathbf{d}_{n+1}$ and Lagrange multipliers $\boldsymbol{\lambda}_{n+1}$ fulfill the Karush-Kuhn-Tucker optimality conditions, e.g., (Bonnans *et al.* 2006),

$$
\begin{aligned}
\nabla_{\mathbf{d}}\mathcal{L}_{n+1}(\mathbf{d}_{n+1}, \boldsymbol{\lambda}_{n+1}) &= \nabla\Pi_{n+1}(\mathbf{d}_{n+1}) + \mathbf{C}^{\mathrm{T}}\boldsymbol{\lambda}_{n+1} = \mathbf{0}, \\
\nabla_{\boldsymbol{\lambda}}\mathcal{L}_{n+1}(\mathbf{d}_{n+1}, \boldsymbol{\lambda}_{n+1}) &= \mathbf{C}\mathbf{d}_{n+1} = \mathbf{0}.
\end{aligned}
\tag{28}
$$

2.3.4 Solution procedure

The resulting system of nonlinear equations is linearized and solved iteratively via the Newton method. The $(k+1)$-th value of nodal displacements is expressed as

$$
{}^{k+1}\mathbf{d}_{n+1} = {}^{k}\mathbf{d}_{n+1} + {}^{k+1}\delta\mathbf{d},
\tag{29}
$$

where the k-th iterate of nodal displacements ${}^{k}\mathbf{d}_{n+1}$ is known and it is set to $\mathbf{d}_n$ at the beginning of the new iteration step. The displacement increment ${}^{k+1}\delta\mathbf{d}$ is determined together with the vector of Lagrange multipliers ${}^{k+1}\boldsymbol{\lambda}$ from the linearized system

$$
\begin{bmatrix} {}^{k}\mathbf{K} & \mathbf{C}^{\mathrm{T}} \\ \mathbf{C} & \mathbf{0} \end{bmatrix} \begin{bmatrix} {}^{k+1}\delta\mathbf{d} \\ {}^{k+1}\boldsymbol{\lambda} \end{bmatrix} = -\begin{bmatrix} {}^{k}\mathbf{f}_{int} - \mathbf{f}_{ext} \\ \mathbf{0} \end{bmatrix}.
\tag{30}
$$

The stiffness matrix and the nodal internal forces are computed from the previous k-th iterate values of nodal displacements

$$
{}^{k}\mathbf{K} = \nabla^2\Pi_{int,n+1}\left({}^{k}\mathbf{d}_{n+1}\right), \quad {}^{k}\mathbf{f}_{int} = \nabla\Pi_{int,n+1}\left({}^{k}\mathbf{d}_{n+1}\right),
\tag{31}
$$

see Appendix A, whereas the nodal external forces $\mathbf{f}_{ext} = \mathbf{f}_{ext,n+1}$ are expressed for the loading level corresponding to the time t_{n+1}.

The iterative procedure is summarized in Algorithm 1, where the residual in the termination criterion is given by the norm of residual forces including the influence of the Lagrange multipliers according to Eq. (28)

$$
{}^{k}\eta = \frac{\| {}^{k}\mathbf{f}_{int} - \mathbf{f}_{ext} + \mathbf{C}^{\mathrm{T}} {}^{k}\boldsymbol{\lambda}\|_2}{\max(\|\mathbf{f}_{ext}\|_2, 1)}.
\tag{32}
$$

The proposed layer-wise model was implemented according to this formulation in the MATLAB system version R2015b, where the tolerance ϵ for the residual ${}^{k}\eta$ in the termination criterion was set to 10^{-5}.

3. Verification and comparisons

Our verification study is performed in detail on an example representing a common loading and boundary conditions for laminated glass plate structures. For laminated glass beams, the case study focusing on the effects of different boundary conditions, loading and temperature is presented in (Zemanová *et al.* 2017). A

Algorithm 1 One step of the exponential algorithm

Data:
tolerance ϵ, load $\mathbf{f}_{ext,n+1}$, displacements $\mathbf{d}_n$, internal forces $\mathbf{n}_n^{(2)}$, $\mathbf{m}_n^{(2)}$, $\mathbf{v}_n^{(2)}$, Maxwell chain stresses $[\sigma_{m,p,e}^n,$ $\sigma_{m,p,e}^m,$ $\tau_{p,e}]_{p=1,e=1}^{P,N_e}$ for $i=2$ and t_n
Initiation:
$k \leftarrow 0$, ${}^0\mathbf{d} \leftarrow \mathbf{d}_n$, ${}^0\delta\mathbf{d} \leftarrow \mathbf{0}$, assemble ${}^k\mathbf{f}_{int}$ and $\mathbf{C}$ in Eq. (31) and Eq. (27)
while $\left({}^k\eta > \epsilon\right)$ **do** assemble ${}^k\mathbf{K}$ from Eq. (31) solve for $\left({}^{k+1}\delta\mathbf{d}, {}^{k+1}\lambda\right)$ from Eq. (30) ${}^{k+1}\mathbf{d}_{n+1} \leftarrow {}^k\mathbf{d}_{n+1} + {}^{k+1}\delta\mathbf{d}$ assemble ${}^{k+1}\mathbf{f}_{int}$ from Eq. (31) $k \leftarrow k+1$
$\mathbf{d}_{n+1} \leftarrow {}^{k+1}\mathbf{d}_{n+1}$
update internal forces from Eq. (18) and Maxwell chain stresses from Eq. (15)

Table 1 Generalized Maxwell series description of the shear relaxation modulus for PVB, after (Andreozzi *et al.* 2014), $G_\infty = 0$ Pa

p	G_p [Pa]	θ_p [s]	p	G_p [Pa]	θ_p [s]
1	1066280	1.00E-01	6	104767	7.25E+03
2	560438	5.89E-01	7	134158	7.56E+04
3	279509	4.32E+00	8	135411	7.38E+05
4	135178	4.00E+01	9	111062	1.10E+07
5	87014	5.31E+02	10	125984	1.00E+08

validation study for laminated glass plates with different types of glasses and polymer interlayers with different boundary conditions and loading scenarios will be discussed in a subsequent paper.

3.1 Problem description

For verification purposes, a square $1.2\,\text{m} \times 1.2\,\text{m}$ three-layered simply supported plate composed of two glass layers (6 mm thick) and a PolyVinyl Butyral (PVB) interlayer (1.52 mm thick) was analyzed. Due to the symmetry, only one quarter of the plate was considered in numerical simulations.

The material parameters were taken from (Andreozzi *et al.* 2014). In particular, the Young modulus $E = 70$ MPa and the Poisson ratio $\nu = 0.22$ are assumed for the linear elastic behavior of glass. The parameters of the chain model to describe the frequency-dependent behavior of the PVB foil are stored in Table 1. The parameters for the time/temperature shift, Eq. (10), $C_1 = 12.1$ and $C_2 = 82$ correspond to the reference temperature $T_0 = 30°C$.

The plate was loaded with a uniform pressure $1,400\,\text{N/m}^2$ during the time period 10^6 s at the temperature of $35°C$. This approximately 12-day-long time interval was divided into time steps defined by fifteen-time instants t_true = [0, 0.1, 0.1778, 0.3162, 0.5623, 1, 1.778, 3.162, 5.623, 10, 10^2, 10^3, 10^4, 10^5, 10^6] s. These values are distributed in

Table 2 Convergence of the central deflection and the maximum principal stresses occurring on the bottom surface of laminated glass pane at the center and near the corner (in the distance $1/10$ of the span from both edges) upon uniform mesh refinement for the problem from Section 3.1

number of elements	5×5	15×15	30×30	40×40	50×50
error in central deflections	1.14%	0.07%	0.01%	0.00%	–
error in stresses at the center	1.28%	0.04%	0.02%	0.01%	–
error in stresses near the corner	5.92%	1.81%	0.64%	0.16%	–

three time intervals uniformly in the logarithmic scale. More specifically, 5 time steps were used to discretize the time intervals $\langle 10^{-1}; 10^0 \rangle$ and $\langle 10^0; 10^1 \rangle$, whereas the time interval $\langle 10^1; 10^6 \rangle$ was divided into 6 time steps. Due to the temperature effects, the time values have to be shifted by parameter a_T, Eq. (10).

The uniform loading was applied to the top surface of laminated glass plate in one second and left constant after that. The corresponding relative magnitude function m simulates the rapid loading increment at the beginning

$$m(t_\text{true}) = \begin{cases} t_\text{true} & \text{for } t_\text{true} \leq 1\text{ s,} \\ 1 & \text{otherwise.} \end{cases} \tag{33}$$

3.2 Convergence

The mesh was refined uniformly, and the convergence of the response of the proposed model was tested for the problem from the previous section. In Table 2, the largest absolute values of the percentage error of the layer-wise model response for different mesh densities are listed; the results are compared with the reference value for the mesh density 50×50 elements.

The central deflections and the maximum principal stress at the center of the bottom surface exhibit a rapid convergence. Due to the geometric nonlinearity, the redistribution of stresses occurs. The largest value of the maximum principal stresses become localized near the corner in a small area, so that the convergence of the maximal principal stress on the bottom surface near the corner (in the distance $1/10$ of the span from both edges) shows significant mesh-dependency. Therefore, we can achieve the results with an engineering accuracy about 1% for the mesh density 25×25 elements for our task. However, we used a finer mesh 50×50 elements for verification purposes. These results are fully in agreement with those found for laminated glass plates with the interlayer modeled as an elastic material, see (Zemanová *et al.* 2015) for more information and graphs.

3.3 Verification

Herein, the proposed layer-wise model, labeled LW–VK–ν, was compared with the response of a three-dimensional model for the problem described in Section 3.1. The detailed 3D analysis was performed using the finite element program – ADINA system 9.2.2 (by
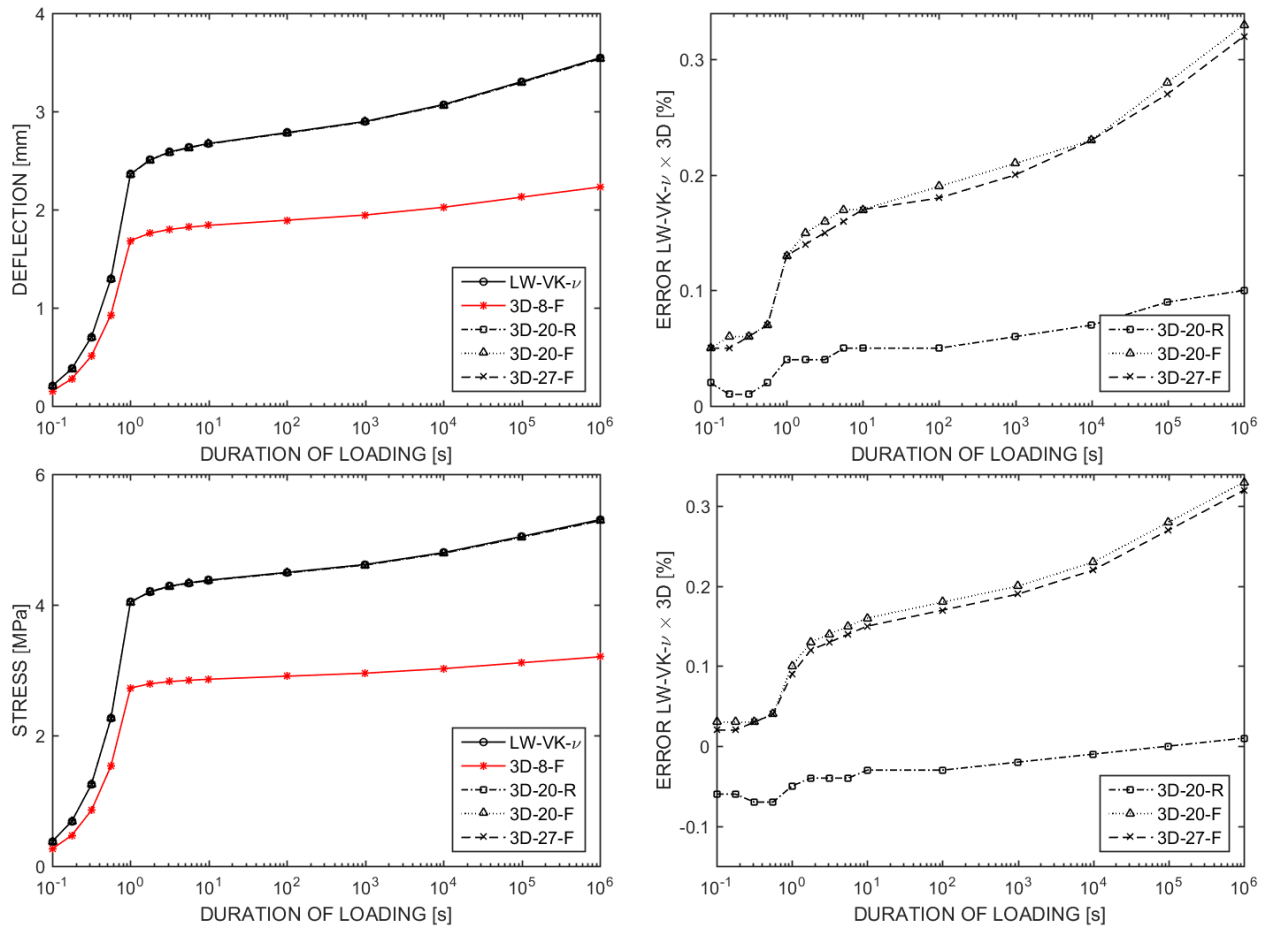
Fig. 2 The time-responses of the layer-wise model LW–VK–ν or 3D-models (Table 3) in terms of the deflections at the center of the plate, the maximum principal stress occurring on the bottom surface of a laminated glass pane near the corner (in the distance of $1/10$ of the span from both edges), and the errors of the LW–VK–ν response against the 3D-models
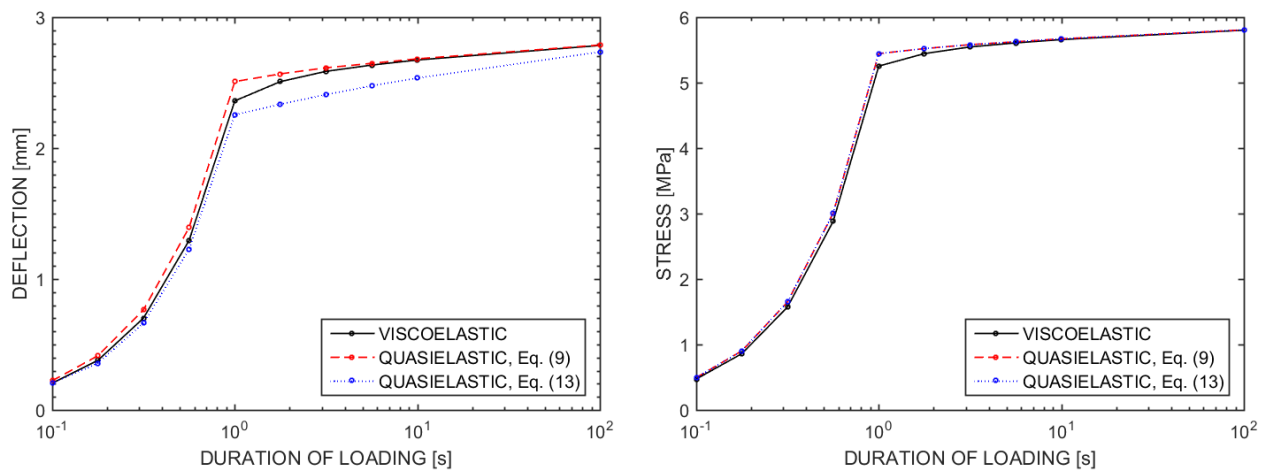

Fig. 3 The relaxation effects demonstrated by the comparison of deflections and maximum principal stresses at the center of the bottom surface of the laminated glass plate from Section 3.1 for quasielastic/viscoelastic behavior of PVB foil

ADINA R&D, Inc.). Five different brick hexahedral elements from the ADINA solver were tested for modeling of laminated glass plates response, see Table 3.

The surface of one quarter of the plate was divided into 50×50 elements for both layer-wise and hexahedral models. Three brick elements were used through the thickness of each glass layer, two for the interlayer, whereas only one element through the thickness of each layer was
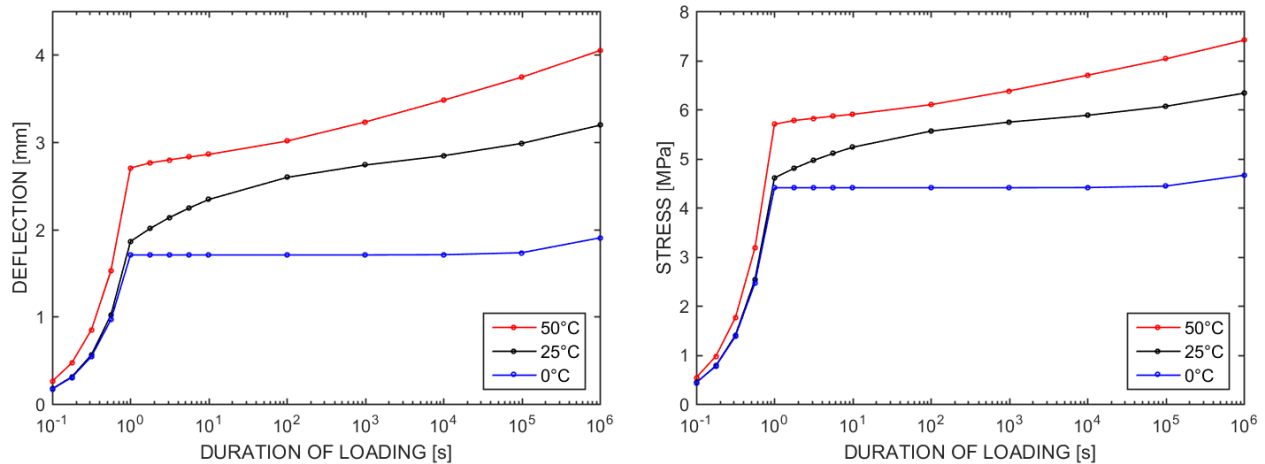
Fig. 4 The effects of temperature and loading time demonstrated on deflections and maximum principal stresses at the center of the bottom surface of the laminated glass plate from Section 3.1

Table 3 The list of brick finite elements used in the ADINA solver

abbreviation	nodes per element	integration type	Gauss points
3D–8–F	8	full	$2 \times 2 \times 2$
3D–20–R	20	reduced	$2 \times 2 \times 2$
3D–20–F	20	full	$3 \times 3 \times 3$
3D–27–F	27	full	$3 \times 3 \times 3$

considered for the layer-wise model. In both analyses, the von Kármán assumptions for large deflections and the constant Poisson ratio were used.

The largest value of deflection and the maximum principal stress occurring on the bottom surface of laminated glass pane near the corner (in the distance $1 / 10$ of the span from both edges) are plotted for each time step in Fig. 2 (on the left). The principal stresses at the node were averaged from values in corresponding elements around the node. Because the response of the layer-wise model is almost indistinguishable from the results of some 3D-models, the relative percentage errors of the layer-wise model compared to the relevant 3D-model are also shown (on the right).

There is a discrepancy between the response of 3D–8–F model and the results of the others. The fully integrated 8-node hexahedral model is too stiff due to the shear locking and delivers inaccurate response; the largest value of percentage error is about 60% for both displacements and stresses. This model is not able to handle large aspect ratio (up to 1:16:16 in our case); the explanation can be found for example in (Petr Krysl 2015).

On the other hand, a very good agreement was found for the responses of the proposed layer-wise model LW–VK–ν and the 20-node or 27-node models (3D–20–R, 3D–20–F, 3D–27–F). The largest values of percentage errors are about 0.1% for 3D-20-R using the reduced integration scheme and about 0.3% for the fully integrated models 3D–20–F and 3D–27–F for deflections and stresses. As is known, the reduced integration, giving a less constrained model, lead to better results for thin plates even for a lower number of elements. The difference between the 3D–20–F and 3D–27–

F responses is negligible, but the 3D–27–F model is significantly more computationally expensive.

The sum of nodal unknowns was 54,621 generalized displacements and Lagrange multipliers in total in case of the layer-wise model, 70,227 displacements for the 8-node 3D-model, 270,351 displacements for the 20-node 3D-model, and 520,251 displacements for the 27-node 3D-model. The computational cost of numerical models corresponds to the above-mentioned numbers of unknowns. The computational time was less than half an hour for the layer-wise model LW–VK–ν in our unoptimized MATLAB solver, two hours for the 20-node 3D-model, and five hours for the 27-node 3D-model in ADINA solver on the same computer.

3.4 Parametric study

The numerical simulations from this section were performed in the developed layer-wise finite element solver in MATLAB. The effects of temperature, load duration, and relaxation effects are briefly demonstrated by a few examples.

In Fig. 3, the comparison of models assuming quasielastic and viscoelastic behavior of the interlayer is presented. For quasielastic models, the analysis reduces to a series of elastic calculations, where we compute the response using constant values of shear modulus for given time instants and do not take into account the stress relaxation. In the first case, the constant value of shear modulus is computed directly from the Prony series in (9). In the second case, we use the effective shear modulus from (13). Responses of the two quasielastic predictions are plot in the graphs:

• Firstly, we approximated the shear modulus of the PVB foil with the equivalent value according to (9). This simplified formulation is widely used in the design practice. The largest values of the error (6–10% for the central deflections and 4–5% for the maximum principal stresses) appear during the rapid load increment in the time interval 10^{-1} s − 1 s, decrease during the constant loading, and stabilize at values smaller than 0.5% at the end of the loading.
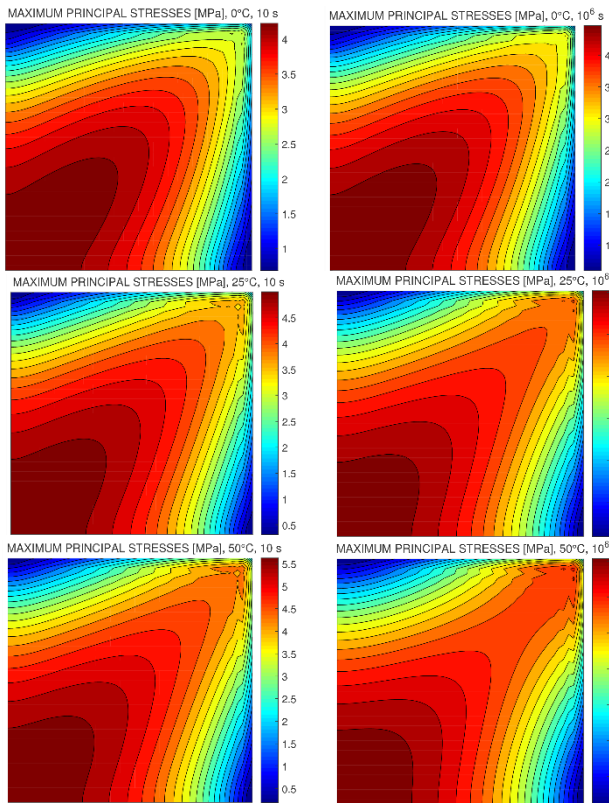
Fig. 5 The effects of temperature and loading time demonstrated on the contours of the maximum principal stresses on the bottom surface of the laminated glass plate from Section 3.1 for duration of loading 10 s or 10^6 s and the ambient temperature 0°C, 25°C, or 50°C

• Then, we also checked the prediction of the quasielastic formulation using the effective shear modulus according to (13) but neglecting the stress relaxation effects from (14). This quasielastic prediction is not on the side of safety even for constant loading; it undervalues the viscoelastic response approximately by 5%.

Note that for loading with loading/unloading parts, the viscoelastic effects are more significant, see (Galuppi and Royer-Carfagni 2013b) and (Zemanová *et al.* 2017).

The effects of the time/temperature-dependency of the PVB foil are demonstrated in Figs. 4 and 5. The time/temperature-dependent behavior of the PVB foil affects the values of quantities of interest, Fig. 4, and partly their distribution as well, Fig. 5, which is caused by the redistribution of stresses due to the geometrically non-linear behavior of plate.

For the central deflections in Fig. 4, the largest values at the end of loading are doubled due to the different temperature, they are about 2 mm for 0°C, 3 mm for 25°C, and 4 mm for 50°C; for the maximum principal stresses at the center of the bottom surface in Fig. 4, the relative errors are slightly smaller. For lower temperature, the values are almost constant and the increase in values is visible for loading duration exceeding 10^5 s. For room and higher temperature, the significant increase in values during the time is visible for both deflections and stresses.

In Fig. 5, the contours of the maximum principal stresses on the bottom surface of one quarter of the plate are plotted for different loading times and temperatures. The top and right edge was modeled as simply-supported; the symmetry boundary conditions were prescribed for the bottom and left edge. For low temperature, the contours are almost the same for 10 s and 10^6 s; for room and higher temperature, there are small differences. In our testing example, the largest value of the maximum principal stress remains at the center of plate. The intensity of loading corresponds to the deflection of 1 / 300 of the span of plate for the largest temperature 50°C at 10^6 s; for higher loading intensity, the differences in graphs would be more significant. More details on the stress redistribution due to the geometric non-linearity for elastic plates can be found in (Zemanová *et al.* 2015).

4. Conclusions

In this paper, the layer-wise theory was applied to examine the behavior of laminated glass plates. The formulation of a geometrically nonlinear multi-layered plate combining stiff elastic material with soft time/temperature-dependent interlayers was performed under the von Kármán assumptions for large deflections with the constant Poisson ratio entering the constitutive equations. This model was verified against 3D simulations in ADINA solver using 8-node, 20-node, and 27-node hexahedral brick elements with reduced or full numerical integration. Further, the computational cost, the relaxation effects, and the time/temperature-dependency of the results were demonstrated with examples and discussed. Based on this comparison, the following conclusions can be made:

• The layer-wise model for laminated glass plates gives very accurate results and reduces the computational time significantly.

• The best agreement was achieved with the 20-node hexahedral finite element model with the reduced integration scheme, which is well-known for its good performance for modeling thin plates under bending. A very good agreement was also found for the fully integrated models using 20-node or 27-node brick elements. The difference in the results of these two models was negligible, but the 27-node finite element model doubled the computational time.

• The viscoelastic effects are significant for loading with changing intensity; for long-term constant loading, the error of the quasielastic solution decreased from the initial value of 5-10% to 0.5%.

• The effects of temperature on the behavior of the PVB foil and therefore the whole laminated glass plate response were significant; the value of the central deflection for 0°C is one half of that for 50°C for the present example.

References

Andreozzi, L., Briccoli Bati, S., Fagone, M., Ranocchiai, G. and

Zulli, F. (2014), "Dynamic torsion tests to characterize the thermo-viscoelastic properties of polymeric interlayers for laminated glass", *Constr. Build. Mater.*, **65**, 1–13.

Belytschko, T., Tsay, C.S. and Liu, W.K. (1981), "A stabilization procedure for the quadrilateral plate element with one-point quadrature", *J. Numer. Meth. Eng.*, **19**(3), 405–419.

Bonnans, J.F., Gilbert, J.C., Lemarechal, C. and Sagastizábal, C.A. (2006), *Numerical Optimization: Theoretical and Practical Aspects*, Springer Science & Business Media, Berlin, Germany.

Carrera, E. (2002), "Theories and finite elements for multilayered, anisotropic, composite plates and shells", *Arch. Comput. Meth. Eng.*, **9**(2), 87–140.

Carrera, E. (2004), "On the use of the Murakami's zig-zag function in the modeling of layered plates and shells", *Comput. Struct.*, **82**(7-8), 541-554.

Christensen, R. (1982), T*heory of Viscoelasticity: An Introduction*, Academic Press, New York, U.S.A.

Duser, A., Jagota, A. and Bennison, S. (1999), "Analysis of glass/polyvinyl butyral laminates subjected to uniform pressure", *J. Eng. Mech.*, **125**(4), 435-442.

Eisenträger, J., Naumenko, K., Altenbach, H., and Köppe, H. (2015a), "Application of the first-order shear deformation theory to the analysis of laminated glasses and photovoltaic panels", *J. Mech. Sci.*, **96-97**, 163-171.

Eisenträger, J., Naumenko, K., Altenbach, H. and Meenen, J. (2015b), "A user-defined finite element for laminated glass panels and photovoltaic modules based on a layer-wise theory", *Compos. Struct.*, **133**, 265-277.

Flocker, F.W. and Dharani, L.R. (1998), "Modeling interply debonding in laminated architectural glass subject to low velocity impact", *Struct. Eng. Mech.*, **6**(5), 485-496.

Galuppi, L. and Royer-Carfagni, G. (2012), "The effective thickness of laminated glass plates", *J. Mech. Mater. Struct.*, **7**, 375-400.

Galuppi, L. and Royer-Carfagni, G. (2013a), "The effective thickness of laminated glass: Inconsistency of the formulation in a proposal of EN-standards", *Compos. Part B Eng.*, **55**, 109-118.

Galuppi, L. and Royer-Carfagni, G. (2013b), "The design of laminated glass under time-dependent loading", *J. Mech. Sci.*, **68**, 67-75.

Huang, X., Liu, G., Liu, Q. and Bennison, S.J. (2014), "An experimental study on the flexural performance of laminated glass", *Struct. Eng. Mech.*, **49**(2), 261-271.

Krysl, P. (2015), *Finite Element Modeling with Abaqus and Matlab for Thermal and Stress Analysis*, Pressure Cooker Press, San Diego, California, U.S.A.

Liang, Y., Lancaster, F. and Izzuddin, B.A. (2016), "Effective modelling of structural glass with laminated shell elements", *Compos. Struct.*, **156**, 47-62.

Mau, S.T. (1973), "A refined laminated plate theory", *J. Appl. Mech.*, **40**(2), 606–607.

Naumenko, K. and Eremeyev, V.A. (2014), "A layer-wise theory for laminated glass and photovoltaic panels", *Compos. Struct.*, **112**, 283-291.

Pica, A., Wood, R.D. and Hinton, E. (1980), "Finite element analysis of geometrically nonlinear plate behaviour using a Mindlin formulation", *Comput. Struct.*, **11**(3), 203-215.

Reddy, J.N. and Robbins, J.D.H. (1994), "Theories and computational models for composite laminates", *Appl. Mech. Rev.*, **47**, 147-169.

Schmidt, J., Zemanová, A., Janda, T., Zeman, J. and Šejnoha, M. (2017), "Variationally-based effective dynamic thickness for laminated glass beams", *Acta Polytech. CTU Proc. 13*, Prague, September.

Williams, M.L., Landel, R.F. and Ferry, J.D. (1955), "The temperature dependence of relaxation mechanisms in amorphous polymers and other glass-forming liquids", *J. Am. Chem. Soc.*, **77**(14), 3701-3707.

Wu, P., Zhou, D., Liu, W., Lu, W. and Wan, L. (2016), "Three-dimensional elasticity solution of layered plates with viscoelastic interlayers", *Mech. Time-Dep. Mater.*, **21**(3), 307-329.

Xenidis, H., Morfidis, K. and Papadopoulos, P.G. (2015), "A method for predicting approximate lateral deflections in thin glass plates", *Struct. Eng. Mech.*, **53**(1), 131-146.

Zemanová, A., Zeman, J., Šejnoha, M., Zemanová, A., Zeman, J. and Šejnoha, M. (2015), "Finite element model based on refined plate theories for laminated glass units", *Lat. Am. J. Sol. Struct.*, **12**(6), 1158-1181.

Zemanová, A., Zeman, J. and Šejnoha, M. (2017), "Comparison of viscoelastic finite element models for laminated glass beams", *J. Mech. Sci.*, **131-132**, 380-395.

Zhang, Y.X. and Yang, C.H. (2009), "Recent developments in finite element analysis for laminated composite plates", *Compos. Struct.*, **88**(1), 147-157.

Zienkiewicz, O.C., Watson, M. and King, I.P. (1968), "A numerical method of visco-elastic stress analysis", *J. Mech. Sci.*, **10**(10), 807-827.

Zienkiewicz, O.C., Taylor, R.L. and Zhu, J.Z. (2013), *The Finite Element Method: Its Basis and Fundamentals*, Elsevier, Amsterdam, the Netherlands.

CC

A. Numerical aspects

Each layer is discretized by four-node quadrilateral elements. The vector of generalized nodal displacements for j-th node and i-th layer

$$\mathbf{d}_j^{(i)} = [u_{0,j}^{(i)}, v_{0,j}^{(i)}, w_{0,j}^{(i)}, \varphi_{x,j}^{(i)}, \varphi_{y,j}^{(i)}]^{\mathrm{T}} \quad (34)$$

consists of two membrane displacements of mid-surface, a deflection, and two rotations, so that for the e-th element with nodes j=1,2,3,4 we get

$$\mathbf{d}_e^{(i)} = [u_{0,1}^{(i)}, v_{0,1}^{(i)}, w_{0,1}^{(i)}, \varphi_{x,1}^{(i)}, \varphi_{y,1}^{(i)},$$
$$u_{0,2}^{(i)}, \cdots u_{0,4}^{(i)}, v_{0,4}^{(i)}, w_{0,4}^{(i)}, \varphi_{x,4}^{(i)}, \varphi_{y,4}^{(i)}]^{\mathrm{T}}. \quad (35)$$

Each unknown displacement or rotation within an element is approximated as a function of four discrete nodal values

$$[\mathbf{u}_0^{(i)}, w_0^{(i)}, \boldsymbol{\varphi}^{(i)}]^{\mathrm{T}} \approx \sum_{j=1}^4 N_j \mathbf{I} \mathbf{d}_j^{(i)} = \mathbf{N}_e \mathbf{d}_e^{(i)} \quad (36)$$

where N_j are bi-linear shape functions, $\mathbf{I}$ is the 5×5 identity matrix, and $\mathbf{N}_e$ is then the 5×20 matrix storing the element basis functions.

Similarly to (Pica *et al.* 1980), the mid-surface membrane strain components Eq. (4), pseudo-curvatures Eq. (5), and transverse shear strains Eq. (3) are given in terms of nodal displacements, respectively,

$$\boldsymbol{\varepsilon}_{m0}^{(i)} \approx \sum_{j=1}^4 \left(\mathbf{B}_{n,j} + \frac{1}{2} \bar{\mathbf{B}}_{K,j}(\mathbf{d}_j^{(i)}) \right) \mathbf{d}_j^{(i)}$$
$$= \left(\mathbf{B}_{n,e} + \frac{1}{2} \mathbf{B}_{K,e}(\mathbf{d}_e^{(i)}) \right) \mathbf{d}_e^{(i)},$$
$$\boldsymbol{\kappa}^{(i)} \approx \sum_{j=1}^4 \mathbf{B}_{b,j} \mathbf{d}_j^{(i)} = \mathbf{B}_{b,e} \mathbf{d}_e^{(i)}, \quad (36)$$
$$\boldsymbol{\gamma}^{(i)} \approx \sum_{j=1}^4 \mathbf{B}_{s,j} \mathbf{d}_j^{(i)} = \mathbf{B}_{s,e} \mathbf{d}_e^{(i)},$$

where $\mathbf{B}_{\bullet,e} = [\mathbf{B}_{\bullet,1}, \mathbf{B}_{\bullet,2}, \mathbf{B}_{\bullet,3}, \mathbf{B}_{\bullet,4}]$ and the submatrices containing the derivatives of shape functions are written as

$$\mathbf{B}_{n,j} = \begin{bmatrix} \frac{\partial N_j}{\partial x} & 0 & 0 & 0 & 0 \\ 0 & \frac{\partial N_j}{\partial y} & 0 & 0 & 0 \\ \frac{\partial N_j}{\partial y} & \frac{\partial N_j}{\partial x} & 0 & 0 & 0 \end{bmatrix},$$

$$\mathbf{B}_{b,j} = \begin{bmatrix} 0 & 0 & 0 & 0 & \frac{\partial N_j}{\partial x} \\ 0 & 0 & 0 & -\frac{\partial N_j}{\partial y} & 0 \\ 0 & 0 & 0 & -\frac{\partial N_j}{\partial x} & \frac{\partial N_j}{\partial y} \end{bmatrix},$$

$$\mathbf{B}_{s,j} = \begin{bmatrix} 0 & 0 & \frac{\partial N_j}{\partial x} & 0 & N_j \\ 0 & 0 & \frac{\partial N_j}{\partial y} & -N_j & 0 \end{bmatrix},$$

$$\mathbf{B}_{K,j}(\mathbf{d}_j^{(i)}) = \mathbf{B}_\theta(\mathbf{d}_j^{(i)}) \bar{\mathbf{B}}_{K,j} =$$
$$= \begin{bmatrix} \sum_{s=1}^4 w_{0,s}^{(i)} \frac{\partial N_s}{\partial x} & 0 \\ 0 & \sum_{s=1}^4 w_{0,s}^{(i)} \frac{\partial N_s}{\partial y} \\ \sum_{s=1}^4 w_{0,s}^{(i)} \frac{\partial N_s}{\partial y} & \sum_{s=1}^4 w_{0,s}^{(i)} \frac{\partial N_s}{\partial x} \end{bmatrix} \begin{bmatrix} 0 & 0 & \frac{\partial N_j}{\partial x} & 0 & 0 \\ 0 & 0 & \frac{\partial N_j}{\partial y} & 0 & 0 \end{bmatrix}. \quad (38)$$

The expressions in $\mathbf{B}_{K,e}$ are linearly dependent on $\mathbf{d}_e^{(i)}$ whereas the other submatrices are independent of $\mathbf{d}_e^{(i)}$. The values of nodal displacements for the evaluation of the $(k + 1)$-th iterate of shape functions, their derivatives, and internal nodal forces are taken from the previous k-th step in the Newton method, we omitted the symbol k to simplify the notation.

The 2×2 Gauss quadrature, with four integration points $[x_g, y_g]_{g=1}^4$, was used to determine the normal and the bending terms of the internal nodal forces, and 1×1 quadrature at the center for the shear terms. This selective integration scheme treats shear locking. For corner supported plates, a stabilization technique has to be used, e.g., (Belytschko *et al.* 1981), to avoid zero-energy modes. Eq. (31) gives the nodal internal forces in the form

$$\mathbf{f}_{int,e}^{(i)} = \mathbf{f}_{int,n,e}^{(i)} + \mathbf{f}_{int,b,e}^{(i)} + \mathbf{f}_{int,s,e}^{(i)}, \quad (39)$$

where

$$\mathbf{f}_{int,n,e}^{(i)} = \sum_{g=1}^4 \alpha_g \left(\mathbf{B}_{n,e}(x_g, y_g) \right.$$
$$\left. + \mathbf{B}_{K,e}(x_g, y_g, \mathbf{d}_e^{(i)}) \right)^{\mathrm{T}} \mathbf{n}_e^{(i)}(x_g, y_g),$$
$$\mathbf{f}_{int,b,e}^{(i)} = \sum_{g=1}^4 \alpha_g \mathbf{B}_{b,e}^{\mathrm{T}}(x_g, y_g) \mathbf{m}_e^{(i)}(x_g, y_g), \quad (40)$$
$$\mathbf{f}_{int,s,e}^{(i)} = \alpha_0 \mathbf{B}_{s,e}^{\mathrm{T}}(x_0, y_0) \mathbf{v}_e^{(i)}(x_0, y_0),$$

with the nodal forces written as

$$\mathbf{n}_e^{(i)}(x_g, y_g) = h^{(i)} \bar{\mathbf{D}}_m^{(i)} G^{(i)} \left(\mathbf{B}_{n,e}(x_g, y_g) \right.$$
$$\left. + \frac{1}{2} \mathbf{B}_{K,e}(x_g, y_g, \mathbf{d}_e^{(i)}) \right) \mathbf{d}_e^{(i)},$$
$$\mathbf{m}_e^{(i)}(x_g, y_g) = \frac{(h^{(i)})^3}{12} \bar{\mathbf{D}}_m^{(i)} G^{(i)} \mathbf{B}_{b,e}(x_g, y_g) \mathbf{d}_e^{(i)}, \quad (41)$$
$$\mathbf{v}_e^{(i)}(x_0, y_0) = h^{(i)} k^{(i)} \mathbf{I} G^{(i)} \mathbf{B}_{s,e}(x_0, y_0) \mathbf{d}_e^{(i)}.$$

Then, the stiffness matrix from Eq. (31) reads as

$$\mathbf{K}_e^{(i)} = \mathbf{K}_{n,e}^{(i)} + \mathbf{K}_{b,e}^{(i)} + \mathbf{K}_{s,e}^{(i)}, \quad (42)$$

where

$$\mathbf{K}_{n,e}^{(i)} = \sum_{g=1}^4 \alpha_g \left(\left(\mathbf{B}_{n,e}(x_g, y_g) \right. \right.$$
$$\left. + \mathbf{B}_{K,e}(x_g, y_g, \mathbf{d}_e^{(i)}) \right)^{\mathrm{T}} h^{(i)} \bar{\mathbf{D}}_m^{(i)} G^{(i)} \left(\mathbf{B}_{n,e}(x_g, y_g) \right)$$
$$\left. + \mathbf{K}_{\sigma,e}^{(i)}(x_g, y_g) \right),$$
$$\quad (43)$$
$$\mathbf{K}_{b,e}^{(i)}$$
$$= \sum_{g=1}^4 \alpha_g \mathbf{B}_{b,e}^{\mathrm{T}}(x_g, y_g) \frac{(h^{(i)})^3}{12} \bar{\mathbf{D}}_m^{(i)} G^{(i)} \mathbf{B}_{b,e}(x_g, y_g),$$
$$\mathbf{K}_{s,e}^{(i)} = \alpha_0 \mathbf{B}_{s,e}^{\mathrm{T}}(x_0, y_0) h^{(i)} k^{(i)} \mathbf{I} G^{(i)} \mathbf{B}_{s,e}(x_0, y_0),$$

and the initial stress matrix is

$$\mathbf{K}_{\sigma,e}^{(i)}(x_g, y_g)$$
$$= \bar{\mathbf{B}}_{K,e}^{\mathrm{T}}(x_g, y_g) \begin{bmatrix} n_{e,1}^{(i)}(x_g, y_g) & n_{e,3}^{(i)}(x_g, y_g) \\ n_{e,3}^{(i)}(x_g, y_g) & n_{e,2}^{(i)}(x_g, y_g) \end{bmatrix} \bar{\mathbf{B}}_{K,e}(x_g, y_g). \quad (44)$$

For the interlayer, the shear modulus in previous equations is the effective one, Eq. (13), and additional members of the nodal internal forces and the stiffness matrix due to the relaxation effects have to be taken into account, cf. (Zemanová *et al.* 2017). In particular, the increments of nodal forces follow from

$$\Delta \hat{\mathbf{f}}_{int,n,e}^{(2)} = \sum_{g=1}^{4} \alpha_g \left(\mathbf{B}_{n,e}(x_g, y_g) \right.$$
$$\left. + \mathbf{B}_{K,e}(x_g, y_g, \mathbf{d}_e^{(2)}) \right)^{\mathrm{T}} \delta \mathbf{n}_e^{(2)}(t_n, x_g, y_g),$$

$$\Delta \hat{\mathbf{f}}_{int,b,e}^{(2)} = \sum_{g=1}^{4} \alpha_g \mathbf{B}_{b,e}^{\mathrm{T}}(x_g, y_g) \delta \mathbf{m}_e^{(2)}(t_n, x_g, y_g), \tag{45}$$

$$\Delta \hat{\mathbf{f}}_{int,s,e}^{(2)} = \alpha_0 \mathbf{B}_{s,e}^{\mathrm{T}}(x_0, y_0) \delta \mathbf{v}_e^{(2)}(t_n, x_0, y_0),$$

where the history variables are provided by

$$\delta \mathbf{n}_e^{(2)}(t_n, x_g, y_g) = \mathbf{n}_e^{(2)}(t_n, x_g, y_g) + \Delta \hat{\mathbf{n}}_e^{(2)}(x_g, y_g)$$
$$- h^{(2)} \bar{\mathbf{D}}_m^{(2)} \hat{G}^{(2)} \boldsymbol{\varepsilon}_{m0,e}^{(2)}(t_n, x_g, y_g),$$

$$\delta \mathbf{m}_e^{(2)}(t_n, x_g, y_g) = \mathbf{m}_e^{(2)}(t_n, x_g, y_g) + \Delta \hat{\mathbf{m}}_e^{(2)}(x_g, y_g)$$
$$- \frac{(h^{(2)})^3}{12} \bar{\mathbf{D}}_m^{(2)} \hat{G}^{(2)} \boldsymbol{\kappa}_e^{(2)}(t_n, x_g, y_g), \tag{46}$$

$$\delta \mathbf{v}_e^{(2)}(t_n, x_0, y_0) = \mathbf{v}_e^{(2)}(t_n, x_0, y_0) + \Delta \hat{\mathbf{v}}_e^{(2)}(x_0, y_0)$$
$$- h^{(2)} k^{(2)} \mathbf{I} \hat{G}^{(2)} \boldsymbol{\gamma}_e^{(2)}(t_n, x_0, y_0),$$

Finally, the stiffness matrix increment for interlayer reads as

$$\Delta \hat{\mathbf{K}}_{\sigma,e}^{(i)}(x_g, y_g)$$
$$= \bar{\mathbf{B}}_{K,e}^{\mathrm{T}}(x_g, y_g) \begin{bmatrix} \delta n_{e,1}^{(i)}(x_g, y_g) & \delta n_{e,3}^{(i)}(x_g, y_g) \\ \delta n_{e,3}^{(i)}(x_g, y_g) & \delta n_{e,2}^{(i)}(x_g, y_g) \end{bmatrix} \bar{\mathbf{B}}_{K,e}(x_g, y_g) \tag{47}$$

Further details regarding the implementation of general quadrilateral elements of an irregular shape can be found in (Pica *et al.* 1980). With minor adjustments, the formulation can also be extended to triangular elements, e.g., (Zienkiewicz *et al.* 2013).